J. Fluid Mech. (1997), *vol.* 350, *pp.* 97–118. Printed in the United Kingdom

© 1997 Cambridge University Press

Turbulence-induced rectified flows in rotating fluids

By XIUZHANG ZHANG, DON L. BOYER AND HARINDRA J. S. FERNANDO†

Environmental Fluid Dynamics Program, Department of Mechanical & Aerospace Engineering, Arizona State University, Tempe, AZ 85287-6106, USA

(Received 9 January 1996 and in revised form 13 May 1997)

Laboratory experiments dealing with Reynolds stress gradients in shear-free turbulence in homogeneous rotating fluids were conducted to better understand associated physical phenomena. The study was motivated by possible applications to the oceanic environment where such Reynolds stress gradients are ubiquitous (e.g. in the vicinity of the continental shelf break, where turbulence decays away from the boundary). The turbulence was generated by vertical oscillations of a circular shaft with O-ring surface roughness elements; the oscillation axis coincided with the axis of symmetry of the cylindrical test cell.

In the absence of background rotation, the turbulence is strong in the immediate vicinity of the shaft surface and decays with the radial distance, r. The turbulence in the boundary layer is such that $u_r \sim u_\theta \sim w$, where u_r, u_θ, w are the radial, azimuthal and vertical r.m.s. velocity components, respectively. These velocity components are found to be proportional to $S\omega$, where S and ω are the stroke and frequency of the shaft oscillations, respectively, i.e. much the same as for the case of oscillating-grid turbulence, which has been studied extensively.

When background rotation is present, the steady-state turbulent intensity close to the shaft is similar to that of the non-rotating experiments. Away from the shaft, in the central portion of the test cell, large-scale motions containing randomly distributed cyclonic and anticyclonic vortices are developed owing to small local Rossby numbers. In the vicinity of the shaft, a rectified anticyclonic flow U_θ is observed. The magnitude of U_θ is found to be proportional to the characteristic r.m.s. turbulence velocity u, but independent of the rate of background rotation.

Consideration of the equations of motion shows that mean flows should not be expected if background rotation is absent. With rotation, however, the equations indicate that the turbulent stresses can initiate, further develop and then maintain a mean anticyclonic (rectified) flow around the cylinder; the azimuthal momentum equation is shown to play a critical role in the generation of the mean anticyclonic flow.

1. Introduction

Rectified currents, defined as mean flows resulting from time-dependent background forcing, are of importance for geophysical flows because they may influence the movement of aquatic biota and the transport of suspended materials such as pollutants (see, for example, Plumb & McEwan 1978). It has been well documented that background rotation plays a decisive role in the flow rectification process in the vicinity of topographic features such as (i) seamounts (Genin, Noble & Lonsdale 1989; Eriksen 1991; Boyer *et al.* 1991; Zhang & Boyer 1993), (ii) continental shelf breaks and banks (Zimmerman 1978; Butman *et al.* 1982; Maas & Zimmerman 1989*a*, *b*; Garreau &

† Author to whom correspondence should be sent: e-mail J.Fernando@asu.edu.

https://doi.org/10.1017/S0022112097006812 Published online by Cambridge University Press

Mazé 1992; Chen & Beardsley 1995) or (iii) along vertical boundaries (Zhang *et al.* 1993, 1994). These studies focused on cases where the forcing scale of the fluid system (e.g. the tidal excursion or the characteristic scale of the topography) is much larger than the characteristic scale of geostrophic turbulence. Holloway (1987), however, pointed out that rectified currents can result from a complete spectrum of motions including, for example, long- and short-period wind effects. Bretherton & Haidvogel (1976) conducted numerical experiments on turbulence above randomly distributed topographic features in a rotating system. They found that the resulting flows were organized in such a way that anticyclonic mean currents were trapped above elevated topographies, while cyclonic motions were limited within basins. The forcing fields considered by Bretherton & Haidvogel (1976) were random but still of large scale, i.e. the Rossby number of the motion field, based on the velocity scale of the random flow field and the characteristic length of the topographic features, was much less than unity.

Laboratory experiments on small-scale rotating turbulence have been considered by, among others, Bretherton & Turner (1968), McEwan (1973, 1976), Ibbetson & Tritton (1975), Collin de Verdiere (1980), Hopfinger, Browand & Gagne (1982), Dickinson & Long (1983) and Bidokhti & Tritton (1992). One characteristic feature identified by these investigators of rotating turbulence is the generation of large-scale coherent structures by small-scale forcing, and this phenomenon is not typical in the absence of the background rotation. McEwan (1973, 1976) argued that, because of the mixing of absolute angular momentum relative to an inertial system, a rotating turbulent flow tends to develop cyclonic vortices. Hopfinger *et al.* (1982) and Dickinson & Long (1983), among others, found that away from a horizontal grid oscillating vertically, the turbulence intensity decreases, while length scales of the motion increase. They also reported that an initially nearly isotropic turbulent flow can organize into large-scale cyclonic and anticyclonic vortices, but they did not study or report on the generation of mean currents. The generation of coherent structures in rotating three-dimensional turbulence has also been reported by Bartello, Métais & Lesieur (1994) and Métais *et al.* (1995) using direct numerical simulation. Bardina, Ferziger & Rogallo (1985) also conducted numerical experiments on homogeneous turbulence in rotating homogeneous fluids. They found that large-scale motions take the form of inertial waves, and the energy cascade to the smaller scale can be greatly reduced owing to the presence of rotation.

The present communication focuses on obtaining a better understanding of flow rectification in rotating turbulent flows with zero mean shear. In particular, the physical system to be considered is given schematically in figure 1. A cylindrical test cell containing a rigid lid and filled with a homogeneous incompressible fluid rotates uniformly about a vertical axis. Turbulence is generated by an oscillating vertical shaft fitted with roughness elements. It is desired to investigate the nature of the turbulent and mean motion fields developed. For comparison purposes, investigations of the non-rotating case are also of interest.

We assume at the outset that turbulence is generated in the vicinity of the roughness elements mainly due to flow separation around them. Assuming that the test cell is sufficiently large, it is reasonable to assume that $\partial/\partial\theta = 0$ and away from the top and bottom boundaries $\partial/\partial z = 0$, where (r, θ, z) are the cylindrical coordinates shown on figure 1. Considering the purely oscillatory nature of the forcing, one expects that no mean velocity would be forced in the vicinity of the shaft. As will be shown below, however, in the presence of background rotation, a mean flow is generated owing to nonlinear effects, i.e. via the gradients of Reynolds stresses. Such a mean flow is shown not to be expected and, in fact, is not found in corresponding non-rotating flows.

https://doi.org/10.1017/S0022112097006812 Published online by Cambridge University Press

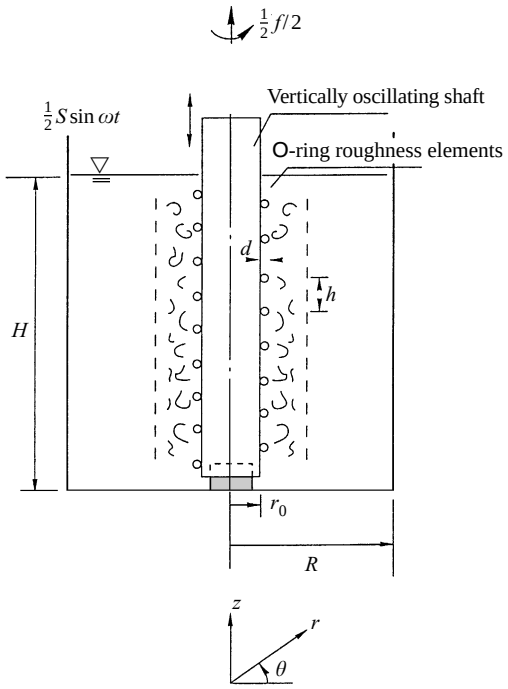


FIGURE 1. Schematic of the experimental facility.

The paper is organized as follows. A theoretical discussion concerning the physical mechanisms at work in the flow rectification process is given in §2. Section 3 describes the laboratory experimental apparatus and various observation and measurement techniques employed. The experimental results are discussed in §4, while concluding remarks and a brief discussion are given in §5.

2. Theoretical considerations

The generation of mean (rectified) flows in rotating fluids by small-scale motions has been discussed by several authors. Scorer (1965, 1966) was the first to point out that small-scale fluctuations may lead to large-scale mean swirls, support for which can be seen in the experiments of Gough & Lynden-Bell (1968), Bretherton & Turner (1968), McEwan (1973, 1976), Hopfinger *et al.* (1982) and Dickinson & Long (1983), among others. A number of mechanisms have been proposed to describe the generation of mean flow by small-scale forcing in rotating flows: some possibilities include the effects of angular momentum mixing (Bretherton & Turner 1968) and vorticity expulsion (Gough & Lynden-Bell 1968). So far no definitive mechanism has been identified and, in what follows, we propose a plausible mechanism in the context of the present experiments. This mechanism may well be embedded in those proposed previously, but an explicit exposition of the proposed mechanism is desirable here.

Consider an axisymmetrical geometry, as shown schematically in figure 1. For simplicity, assume that the turbulence is generated at the rough boundary of an oscillating shaft, and then diffuses away into the outer flow. Assume that any mean flow so generated has velocity components (U_r, U_θ, W). The incompressibility condition requires

$$\frac{\partial U_r}{\partial r}+\frac{U_r}{r}+\frac{1}{r}\frac{\partial U_\theta}{\partial \theta}+\frac{\partial W}{\partial z}=0, \tag{1}$$

https://doi.org/10.1017/S0022112097006812 Published online by Cambridge University Press

or, based on the assumptions $\partial/\partial\theta = 0$ and $\partial/\partial z = 0$,

$$\frac{1}{r}\frac{\partial(rU_r)}{\partial r} = 0 \Rightarrow U_r = \frac{F(t)}{r}, \tag{2}$$

where $F(t)$ is to be determined. Considering that $U_r = 0$ at $r = r_0 + k_R$, where r_0 is the radius of the oscillating cylinder and k_R is a mean equivalent roughness, we conclude that $U_r = 0$ everywhere, for this special configuration. Because W is independent of z and equal to zero at the test cell floor and confining rigid lid, $W = 0$ everywhere.

The momentum equations in the radial, azimuthal and vertical directions can be written as

$$\frac{\mathrm{D}U_r}{\mathrm{D}t} - \frac{U_\theta^2}{r} - fU_\theta = -\frac{1}{\rho}\frac{\partial P}{\partial r} + \nu\left(\nabla^2 U_r - \frac{U_r}{r^2} - \frac{2}{r^2}\frac{\partial U_\theta}{\partial\theta}\right) - \frac{1}{r}\frac{\partial(r\overline{u_r'^2})}{\partial r} - \frac{1}{r}\frac{\partial\overline{u_r' u_\theta'}}{\partial\theta} - \frac{\partial\overline{u_r' w'}}{\partial z} + \frac{\overline{u_\theta'^2}}{r}, \tag{3}$$

$$\frac{\mathrm{D}U_\theta}{\mathrm{D}t} + \frac{U_r U_\theta}{r} + fU_r = -\frac{1}{\rho r}\frac{\partial P}{\partial\theta} + \nu\left(\nabla^2 U_\theta - \frac{U_\theta}{r^2} + \frac{2}{r^2}\frac{\partial U_r}{\partial\theta}\right) - \frac{1}{r}\frac{\partial\overline{u_\theta'^2}}{\partial\theta} - \frac{\partial\overline{u_r' u_\theta'}}{\partial r} - \frac{\partial\overline{u_\theta' w'}}{\partial z} - 2\frac{\overline{u_r' u_\theta'}}{r}, \tag{4}$$

$$\frac{\mathrm{D}W}{\mathrm{D}t} = -\frac{1}{\rho}\frac{\partial P}{\partial z} + \nu\nabla^2 W - \frac{\partial\overline{w'^2}}{\partial z} - \frac{1}{r}\frac{\partial r\overline{u_r' w'}}{\partial r} - \frac{1}{r}\frac{\partial\overline{u_\theta' w'}}{\partial\theta}, \tag{5}$$

respectively, where

$$\frac{\mathrm{D}}{\mathrm{D}t} = \frac{\partial}{\partial t} + U_r\frac{\partial}{\partial r} + \frac{U_\theta}{r}\frac{\partial}{\partial\theta} + W\frac{\partial}{\partial z},$$

$$\nabla^2 = \frac{\partial^2}{\partial r^2} + \frac{1}{r}\frac{\partial}{\partial r} + \frac{1}{r^2}\frac{\partial^2}{\partial\theta^2} + \frac{\partial^2}{\partial z^2},$$

f is the Coriolis parameter, ρ is the density, P is the mean pressure from which gravitational and centrifugal effects associated with the system rotation have been subtracted, ν is the kinematic viscosity, u_r', u_θ' and w' are the velocity fluctuations in the (r, θ, z)-directions and overbars denote averaged quantities.

Neglecting viscous effects, assuming $\partial/\partial z = \partial/\partial\theta = 0$, and using the results $U_r = W = 0$, (3)–(5) can be written as

$$-\frac{U_\theta^2}{r} - fU_\theta = -\frac{1}{\rho}\frac{\partial P}{\partial r} - \frac{\partial\overline{u_r'^2}}{\partial r} - \frac{\overline{u_r'^2}}{r} + \frac{\overline{u_\theta'^2}}{r}, \tag{6}$$

$$\frac{\partial U_\theta}{\partial t} = -\frac{\partial\overline{u_r' u_\theta'}}{\partial r} - 2\frac{\overline{u_r' u_\theta'}}{r}, \tag{7}$$

and

$$0 = -\frac{1}{r}\frac{\partial r\overline{u_r' w'}}{\partial r}, \tag{8}$$

respectively.

First, consider the case of no rotation, i.e. $f = 0$. Symmetry considerations imply that, for this case, the term $\overline{u_r' u_\theta'}$ in (7) must be identically zero for all times. Because $U_\theta(r, t = 0) = 0$, this implies from (7) that

$$U_\theta(r, t) = 0 \tag{9}$$

https://doi.org/10.1017/S0022112097006812 Published online by Cambridge University Press

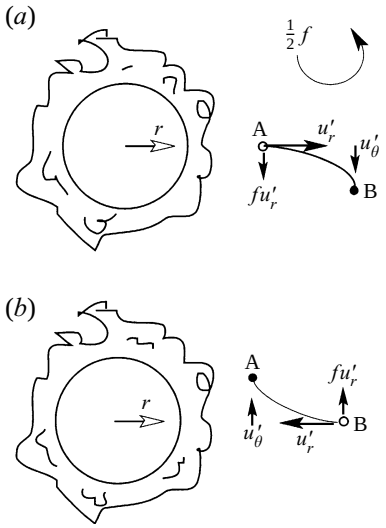


FIGURE 2. Schematic diagram illustrating the tendency for the Reynolds stress $\overline{u'_r u'_\theta} < 0$ for the present physical system.

and from (6) that

$$\frac{\partial P}{\partial r} = \rho\left(-\frac{\partial \overline{u'^2_r}}{\partial r} - \frac{\overline{u'^2_r}}{r} + \frac{\overline{u'^2_\theta}}{r}\right), \tag{10}$$

i.e. the Reynolds stresses are supported by the radial pressure gradient. Some time after the initiation of boundary-induced turbulence, the steady state described by (10) is expected to be reached. By similar arguments as for $\overline{u'_r u'_\theta}$, the term $\overline{u'_r w'} = 0$ and thus relation (8) is also satisfied.

Now consider the case where background rotation is present. Upon initiation of the shaft oscillations, the turbulent front propagates outwards, i.e. the turbulence produced by the shaft diffuses radially. During this phase, the frontal region is sharp, and it is possible to hypothesize that

$$\left|\frac{\partial}{\partial r}\overline{u'_r u'_\theta}\right| \gg 2\left|\frac{\overline{u'_r u'_\theta}}{r}\right|; \tag{11}$$

support for this inequality will be given below. For the purpose of illustrating the mechanism that comes into play in the generation of a mean flow, we combine (11) and (7) to yield

$$\frac{\partial U_\theta}{\partial t} \approx -\frac{\partial}{\partial r}\overline{u'_r u'_\theta}, \tag{12}$$

which shows that the sign and spatial characteristics of $\overline{u'_r u'_\theta}$ are major factors governing the magnitude and the direction of the rectified flow.

To establish the sign of $\overline{u'_r u'_\theta}$, consider the schematic diagram of the turbulent front as given in figure 2(*a*, *b*). For $f > 0$, a parcel initially at position A moving radially outward with velocity u'_r, is subjected to a Coriolis force fu'_r which in turn deflects the parcel in the direction shown towards location B (see figure 2*a*). Consequently a negative u'_θ is to be expected for a positive u'_r. On the other hand, a fluid parcel initially at B moving with a negative velocity u'_r, is expected to experience a positive u'_θ owing to the Coriolis force fu'_r in the direction shown in figure 2(*b*). Thus considering both

https://doi.org/10.1017/S0022112097006812 Published online by Cambridge University Press

positive and negative u_r', one expects $\overline{u_r' u_\theta'} < 0$ for a counterclockwise background rotation. Similarly, the consideration of displacements in the positive and negative θ-directions leads to $\overline{u_r' u_\theta'} > 0$. Given, however, that the turbulent diffusion outward from the source during the flow development phase creates a forward bias for the particle displacements, one may argue that the contributions from the radial displacements dominate the Reynolds stress, and hence $\overline{u_r' u_\theta'} < 0$.

With regard to the spatial distribution of $\overline{u_r' u_\theta'}$, one may hypothesize that $|\overline{u_r' u_\theta'}|$ decreases with increasing r. This follows from the fact that both $u_r (= \overline{u_r'^2}^{1/2})$ and $u_\theta (= \overline{u_\theta'^2}^{1/2})$ decrease with r and the correlation coefficient between u_r' and u_θ' remains essentially unchanged with r.† (As discussed before, in the absence of rotation, this correlation coefficient is approximately zero.) Therefore $\partial \overline{u_r' u_\theta'}/\partial r$ is positive in the vicinity of the turbulent front. One thus expects that $\partial U_\theta/\partial t < 0$ in (12), and a negative U_θ (anticyclonic) is generated.

At large times, a steady-state flow distribution is expected; taking $\partial U_\theta/\partial t = 0$ owing to the assumption of a steady state, one obtains from (7) that

$$-\overline{u_r' u_\theta'} \propto 1/r^2. \tag{13}$$

If the correlation coefficient between u_r and u_θ is constant as discussed above, then

$$u_r \propto 1/r \quad \text{and} \quad u_\theta \propto 1/r, \tag{14}$$

as observed in the present experiments. Further, before the steady-state Reynolds stress gradients are established, the stresses at the frontal region are expected to show faster spatial decay rates, say $-\overline{u_r' u_\theta'} \propto 1/r^m$, with $m > 2$. This argument ensures that the inequality (11) is satisfied during the transient state of the flow.

At this juncture, it is useful to comment on the magnitude of the steady rectified flow generated due to the above mechanism. If the fluid is at rest relative to either a non-rotating or a rotating observer, the radial pressure gradient must vanish, i.e. $\partial P/\partial r = 0$. When the agitations are started, it is expected that $\partial P/\partial r \neq 0$, because there is no physical reason why that pressure gradient should remain zero. As discussed before, when there is no rotation, $U_\theta = 0$, and the radial pressure gradient is in balance with the Reynolds stress gradient according to (10) but, when rotation is added, the terms on the left-hand side of (6) also can play a dominant role in the balance of radial momentum; U_θ can grow according to (12), until a steady state is achieved. If it is assumed that U_θ is a key player in the steady radial momentum balance in the presence of rotation, then (6) implies that the maximum $\partial P/\partial r$ should, at most, be of the order of $\rho u^2/\eta$ where u is the characteristic r.m.s. velocity $u \sim \overline{u_r'^2}^{1/2} \sim \overline{u_\theta'^2}^{1/2} \sim \overline{w'^2}^{1/2}$ and η is the thickness of the turbulent boundary layer. Dickinson & Long (1983) and Hopfinger *et al.* (1982) found that η surrounding a vertically oscillating cylinder, such as considered herein, is given by

$$\eta = \beta u/f, \tag{15}$$

where β is a constant; this condition is synonymous with the turbulent Rossby number within the boundary layer being of order unity.

Using (15) and recognizing that $\partial P/\partial r$ is at most of order $\rho u^2/\eta$, it is possible to obtain a scaling for u_θ from relation (6). If the radius of the oscillating cylinder is of the same order as the boundary layer thickness, as is the case in the present

† Dimensional arguments indicate that this correlation coefficient is a function of the turbulence Rossby number $Ro = u/fl$, where l is the characteristic length scale of the turbulence. Since in rotationally affected turbulent flows Ro is a constant (Hopfinger *et al.* 1982), the correlation coefficient is expected to be a constant.

https://doi.org/10.1017/S0022112097006812 Published online by Cambridge University Press

experiments, then we can write $r \sim \eta$, and hence all of the terms in (6) have a comparable magnitude, leading one to conclude that

$$U_\theta \sim u, \tag{16}$$

i.e. the rectified azimuthal velocity u_θ scales as the characteristic turbulence intensity, independent of the background rotation! (This prediction is supported by the experimental results discussed in §4.2.2). It should also be pointed out that if $r \gg \eta$ then $r \sim r_0$ and, if one hypothesizes that $U_\theta \lesssim u$, then it is possible to obtain the same scaling as (16); here the first term on the left and third and fourth terms on the right in (6) become negligible.

In summary, the equations of motion clearly indicate that no mean flow should be expected for the non-rotating case. For the rotating case, however, the Reynolds stresses in the azimuthal momentum equation tend to initiate a clockwise (anticyclonic) mean flow. The anticyclonic flow so generated eventually achieves a steady state. If the radial momentum balance in the steady state is dominated by the azimuthal mean flow, then the velocity of the rectified flow is expected to be proportional to the r.m.s. turbulence intensity.

Finally, it should be noted that the above theoretical inferences are in consonance with the angular momentum mixing arguments advanced by Bretherton & Turner (1968). The absolute angular momentum M_0 can be defined as

$$M_0 = (\tfrac{1}{2}rf + U_\theta)\, r.$$

Relation (7) can be rearranged into

$$\frac{\partial (rU_\theta)}{\partial t} = \frac{\partial}{\partial t}(M_0) = -\frac{1}{r}\frac{\partial}{\partial r}[r(\overline{ru_r' u_\theta'})]. \tag{17}$$

Note that the term $\partial(rU_\theta)/\partial t$ can be considered as the rate of change of the mean angular momentum for a non-rotating observer. The term $r\overline{u_r' u_\theta'}$ can thus be interpreted as the mean radial flux of angular momentum (see Bretherton & Turner 1968) because

$$r\overline{u_r' u_\theta'} = \overline{ru_r'(u_\theta' + U_\theta + \tfrac{1}{2}rf)}, \tag{18}$$

where the terms in the bracket represents the absolute azimuthal velocity of a fluid parcel relative to the non-rotating system. Bretherton & Turner (1968) found that the right-hand side of (18) has a negative value, which is in agreement with our earlier determination that $\overline{u_r' u_\theta'} < 0$.

3. Experimental facilities and measurement techniques

The experiments were conducted in a cylindrical Plexiglas tank, having a radius $R = 30$ cm and height $H = 50$ cm, respectively (see figure 1). The cylindrical tank is encased within a rectangular Plexiglas tank to prevent optical distortion in flow visualization experiments. A hollow circular Plexiglas shaft with outer radius $r_0 = 4.45$ cm was mounted along the tank axis. The shaft surface, over a 45 cm length, was rapped with plastic-coated copper wires of diameter $d = 0.5$ cm in an O-ring shape with a spacing $h = 2$ cm. These coated wires served as the roughness elements for generating turbulence in the vicinity of the shaft. The top of the shaft was connected to a linear bearing and was driven by a DC motor, thus forcing the shaft to oscillate vertically in a sinusoidal manner. The stroke S (twice the amplitude) and the oscillation frequency ω could be varied in the ranges $0 \leqslant S \leqslant 3.4$ cm and $3 \leqslant \omega \leqslant 25$ rad s^{-1}.

https://doi.org/10.1017/S0022112097006812 Published online by Cambridge University Press

Parameter	Description	Values
H	Depth of fluid	50 cm
R	Radius of tank	30 cm
ν	Kinematic viscosity	0.01 cm^2 s^{-1}
r_0	Shaft radius	4.45 cm
d	Width of roughness elements	0.5 cm
h	Vertical spacing of O-ring roughness	2.0 cm
S	Stroke of shaft oscillation	1.0 – 3.4 cm
ω	Frequency of shaft oscillation	3.1–25.0 rad s^{-1}
f	Coriolis parameter	0–1.6 rad s^{-1}
Ro_t	Temporal Rossby number	2–120 and ∞
Re_s	Shaft Reynolds number	150–4000

TABLE 1. Experimental parameters

Defining a temporal Rossby number $Ro_t = \omega/f$ and a Reynolds number $Re_s = d\omega S/\nu$ for the shaft oscillations, the experiments were carried out in the ranges $2 \lesssim Ro_t \lesssim 120$ (as well as $Ro_t = \infty$ for the non-rotating experiments) and $150 \lesssim Re_s \lesssim 4000$.

The tank, shaft and driving mechanism were mounted on a turntable capable of rotating at a constant rate up to $f/2 = 1.0$ rad s^{-1}. The working fluid was water and the room temperature was about 25 °C. Secondary motions induced near the bottom of the shaft were negligible (this will be discussed subsequently). In order to facilitate flow diagnostics, the upper surface of the fluid was covered by a Plexiglas plate. Detailed dimensions of the facility and the ranges of the parameters investigated are given in table 1.

Turbulent and mean velocities were measured by using a two-component fibre optics laser-Doppler anemometer (LDA), mounted on the turntable; the LDA can be operated in either forward- or backward-scatter modes. The forward-scatter mode of the LDA was used and the resulting signals were stored in a PC for later analysis. The sampling times were varied between 50 s and 120 s, with typically 3000–7500 samples recorded at a given location.

Four flow visualization techniques were used: dye tracers, the electrolytic precipitation method (Honji, Taneda & Tatsuno 1980), neutrally buoyant particles and rheoscopic particles. The electrolytic precipitation technique is used on the observation that when a small DC voltage (~ 5 V) is applied between a solder cathode and, say, a brass anode in an electrically conducting liquid, a white colloidal cloud is released from the solder. In the experiments, a small amount of salt was added to the water to improve its electrical conductivity. The neutrally buoyant particles used were polystyrene beads of nominal diameter 0.5 mm and approximate density 1.043 $(10)^3$ kg m^{-2}; these particles remained suspended in water with its density adjusted by adding an appropriate amount of salt. Rheoscopic particles align with the local velocity shear so as to produce bright and dark structure (patterns). This method was found to be useful in identifying the approximate boundary between the turbulent boundary layer region near the shaft and the outer, seemingly laminar, motion field. Light sheets of thickness 0.5–1.0 cm were employed for illumination in all of the above flow visualization techniques. Two 35 mm cameras, attached to the rotating frame, were used to record the flow patterns. For the experiments with neutrally buoyant particles, the light sheets were 'chopped' appropriately to yield single dot-dash particle streak patterns, with the flow direction being from dot to dash. Both the light sheets and cameras were controlled using a computer.

https://doi.org/10.1017/S0022112097006812 Published online by Cambridge University Press

4. Experimental results

4.1. *Turbulence without background rotation*

Upon initiation of the shaft oscillations in the non-rotating experiments, vortices were generated in the immediate vicinity of the roughness elements mainly due to the flow separation at these elements. These vortices then interacted with each other and quickly moved away from the shaft, forming a turbulent front. The front then propagated radially outward. From particle streak observations it was apparent that the turbulence intensity decreases with increasing distance from the shaft. At large times, the flow field reached a quasi-steady state, i.e. the turbulence intensity at a fixed location did not show appreciable variation with time. In a series of non-rotating and rotating laboratory experiments, Dickinson & Long (1983) reported on turbulence generated by a vertically oscillating rod with roughness elements. If we use the radial turbulence propagation speed obtained by these investigators, it is estimated that approximately five minutes should be allowed in the present experiments to achieve a quasi-steady state. On this basis, the measurements were started fifteen minutes after the initiation of the shaft oscillation. Velocity measurements were made after the system reached this quasi-steady state.

As mentioned above, turbulence in the immediate vicinity of the oscillating shaft is generated by a complex vortex shedding and interaction process. Measurements were made to determine whether the initial vortical motions were similar to the wake structure of a cylinder subjected to a uniform approach flow, as is evident from the oscillating-grid experiments of Hopfinger & Toly (1976). At a fixed radial distance (i.e. 0.5 cm away from the O-ring roughness elements), the velocities were measured for various S and ω, and autocorrelations were determined. The prominent frequency peak of an autocorrelation, n, was used to estimate the Strouhal number $St = nd/S\omega$, where d is the width of the O-ring roughness. The measured Strouhal numbers were widely scattered and varied from 0.1 to 2.0, suggesting that the vortical structure in the immediate vicinity of the roughness is much different from that obtained in simple vortex shedding behind a cylinder in a uniform flow. It was apparent that the turbulence was developed by complex interactions between vortices generated by neighbouring roughness elements.

Measurements of the turbulence intensity and mean flow were made along a tank radius at the mid-depth for various S and ω. In the following (u_r, u_θ, w) designate the r.m.s. velocity fluctuations $(\overline{u_r'^2}^{1/2}, \overline{u_\theta'^2}^{1/2}, \overline{w'^2}^{1/2})$, respectively. Figure 3 is a plot of the r.m.s. velocities normalized by $S\omega$ versus the dimensionless radial distance $\gamma = (r - r_0)/d$ for $S = 20$ cm and $\omega = 24.5$ rad s^{-1}. The dashed line is the least-squares fit of a linear function expressed by the relation

$$\frac{(u_r, u_\theta, w)}{S\omega} = \frac{\kappa}{\gamma}, \tag{19}$$

where κ is expected to be a function of S, ω, d and h; for figure 3, $\kappa \approx 0.024$. Note that for $\gamma \lesssim 10$, (19) represents the turbulence decay very well. For $\gamma \gtrsim 10$, the normalized r.m.s. velocities are approximately constant because of the existence of low-frequency motions and instrument error (the measured r.m.s. noise level, normalized by $S\omega$, is approximately 0.005). To compare the results with previous work (e.g. Hopfinger & Toly 1976), the data are plotted on a log–log graph, which is the insert in figure 3: the slope for $\gamma \lesssim 10$ is approximately -1, i.e. similar to oscillating-grid turbulence. Note also that u_r, u_θ and w have similar magnitudes.

The dependence of the turbulent intensity on S and ω was also investigated; the

https://doi.org/10.1017/S0022112097006812 Published online by Cambridge University Press

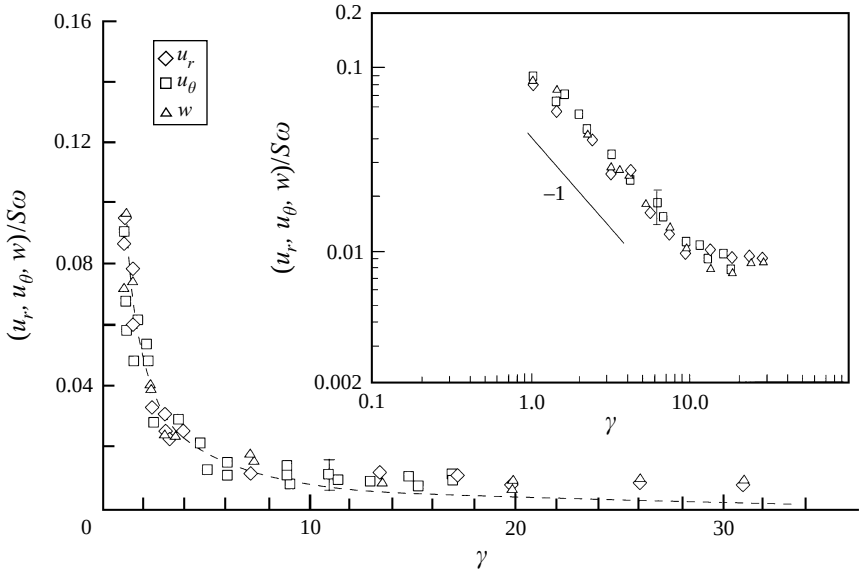


FIGURE 3. Normalized r.m.s. velocities versus the dimensionless distance from the shaft surface for $S = 2.0$ cm, $\omega = 24.5$ rad s^{-1} and $f = 0$ rad s^{-1}. The insert is the log–log plot of the same data. The LDA measurements reported here and below were all taken at mid-fluid depth.

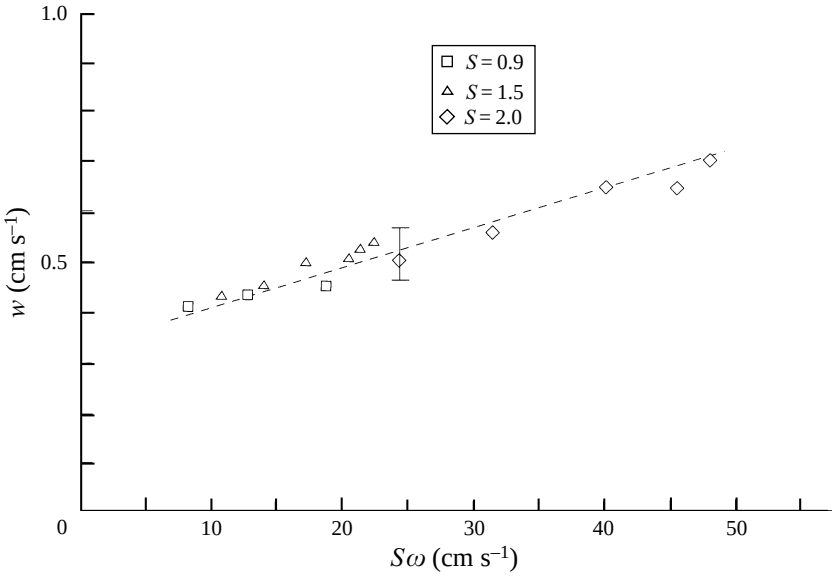


FIGURE 4. Vertical r.m.s. velocity component versus $S\omega$ for a fixed dimensionless distance $\gamma = 3.5$ from the shaft surface and for no background rotation (i.e. $f = 0$ rad s^{-1}).

vertical r.m.s. velocity component was chosen as representative. On physical grounds it was expected that $w/S\omega \sim$ constant so that the data can be presented on a w against $S\omega$ plot (note that this constant depends on the nature of the roughness elements). The data for a fixed radial location $r - r_0 = 1.75$ cm ($\gamma = 3.5$) are plotted on figure 4. The dashed line is a linear regression expressed by

$$w = AS\omega + B, \tag{20}$$

https://doi.org/10.1017/S0022112097006812 Published online by Cambridge University Press

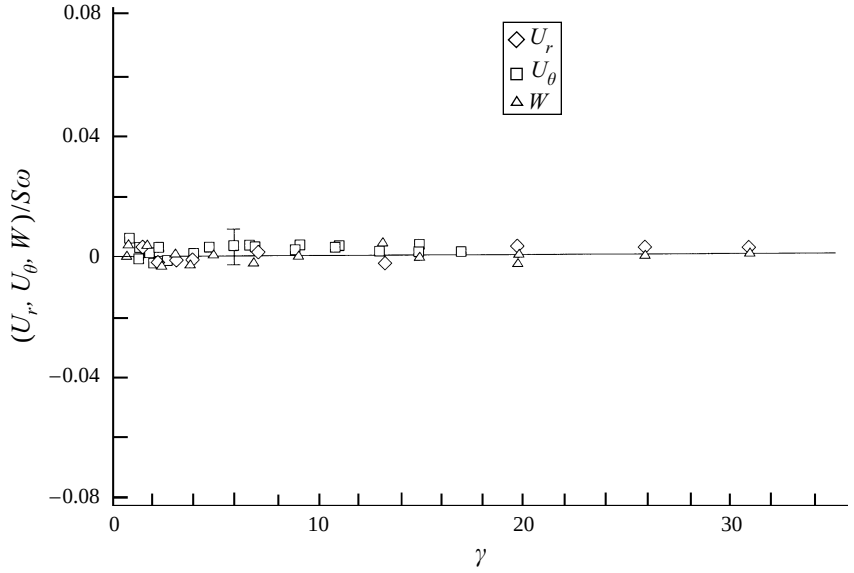


FIGURE 5. Normalized mean velocities versus γ for $S = 2.0$ cm, $\omega = 24.5$ rad s^{-1} and for no background rotation (i.e. $f = 0$ rad s^{-1}).

where $A \approx 0.008$ and $B \approx 0.3$ cm s^{-1}. Note that B need not be zero because (20) is invalid for $\omega = 0$; in fact, the flow is turbulent only above a critical value of ω. The above observations suggest that (i) for the turbulence generated by the oscillating shaft $u_r \sim u_\theta \sim w$ and (ii) the turbulence intensity is linearly dependent on the characteristic speed of the shaft $S\omega$.

The normalized mean velocities $(U_r, U_\theta, W)/S\omega$ are plotted against γ in figure 5 for the same experiments as for figure 3. The mean velocities, within measurement errors, are effectively zero, a result in consonance with the theoretical arguments presented in §2. The estimated error, normalized with $S\omega$, for the time-mean velocities is ± 0.005. These data will be compared below with similar experiments conducted in the presence of background rotation.

Fernando & De Silva (1993) pointed out that certain secondary mean flows could be generated by an oscillating grid in non-rotating fluids when the geometry of the grid is not appropriately constructed, i.e. if the grid produces non-zero Reynolds stress gradients. Accordingly, in the present experiments, secondary flows can be expected in the vicinity of the oscillating shaft near the bottom or near the surface because of locally vertical inhomogeneities in those regions. By introducing rheoscopic particles into the tank, it was observed that indeed some secondary motions are generated in these regions, with the secondary motion near the upper surface being much smaller than that along the tank floor. These secondary motions, however, were limited to regions $\lesssim 5$ cm from the top surface and tank floor. Thus end effects can be considered as negligible when considering the velocity field in the central portions of the fluid. It is concluded that the flow field in the central portions of the tank, say $-20 < z < 20$ cm, is depth independent and that the measurements at $z = 0$ are representative of the motion field throughout the bulk of the fluid column. These same conclusions on depth independence of the motion were also drawn for the experiments conducted in the presence of background rotation.

https://doi.org/10.1017/S0022112097006812 Published online by Cambridge University Press

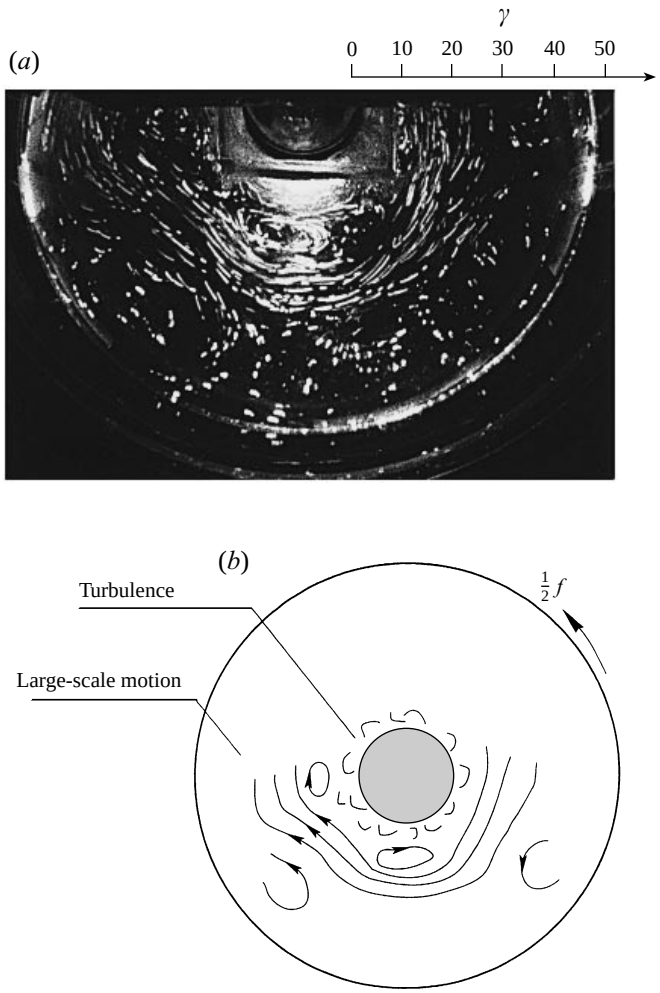


FIGURE 6. (*a*) Top-view photograph of particle streaks for $S = 2.0$ cm, $\omega = 24.5$ rad s^{-1} and $f = 1.6$ rad s^{-1}; the exposure time is 4 s. (*b*) Corresponding interpretive sketch.

4.2. *Turbulence in rotating fluids*

4.2.1. *Qualitative description*

After the fluid in the test cell reached solid-body rotation (after about one hour), the shaft oscillations were started. The observations concerning the generation of turbulence and its propagation away from the shaft surface were similar to those for non-rotating fluids. The larger the radial distance, the weaker the turbulence and the larger the motion length scale. At large radial distances, 'coherent' large-scale motions appeared, indicating the importance of background rotation which has a tendency to transfer energy from small- to large-scale motions. These motions were visualized by using neutrally buoyant particles.

Figure 6(*a*) is a particle streak photograph taken at mid-depth of the fluid for $S = 2.0$ cm, $\omega = 24.5$ rad s^{-1} and $f = 1.6$ rad s^{-1}. The normalized coordinate γ is indicated on the upper-right of the figure. The thickness of the light sheet is ≈ 1 cm. A corresponding interpretive sketch is given in figure 6(*b*), along with an arrow indicating the rotation direction of the tank. Note on figure 6(*a*) that the bright croissant-shaped

https://doi.org/10.1017/S0022112097006812 Published online by Cambridge University Press

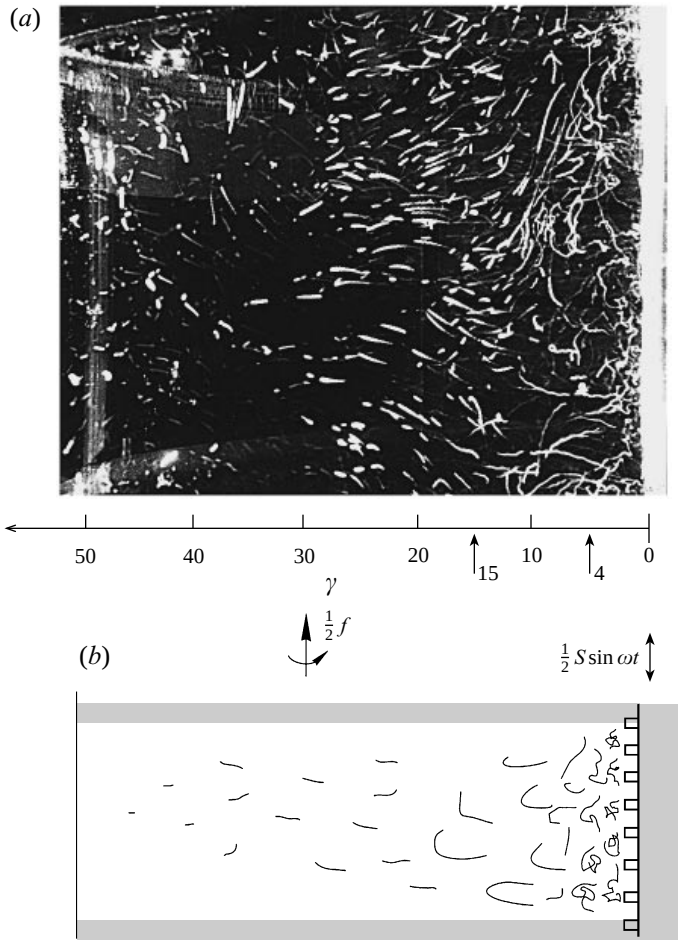


FIGURE 7. (*a*) Side-view photograph of particle streaks for the same experiment as in figure 6(*a*); the exposure time is 4 s. (*b*) Corresponding interpretive sketch.

spot is the reflection of the light sheet from the shaft surface. The motion direction of the particle streaks is from dot to dash as mentioned in §3. It can be seen in figure 6(*a*) that in the vicinity of the shaft the dot-dash patterns of the particles cannot easily be identified because the turbulence in the region is intense and three-dimensional and particles move in and out vertically through the light sheet; this near-shaft region is considered as the turbulent boundary layer. Away from the turbulent layer, the motion is 'organized' into large-scale flows, including anticyclonic and cyclonic vortices, as is evidenced by the dot-dash particle patterns on figure 6(*a*). The typical speed of the particles in the large-scale-motion area is ~ 0.5 cm s^{-1}. From sequential photographs, one observes that the overall structure of the large-scale motion propagates anticyclonically at a speed of approximately 0.3 cm s^{-1}. Taking the typical speed and length scale of the large-scale motion as 0.5 cm s^{-1} and 10 cm, respectively, the Rossby number can be estimated as 0.03. Rotation effects are, therefore, of leading-order importance in the far field. Such large-scale vortices (but not currents) were also reported by Hopfinger *et al.* (1982) and Dickinson & Long (1983) in observations made away from the vertical turbulent boundary layer.

Figure 7(*a*) is a side-view photograph (with the camera angled slightly downward)

https://doi.org/10.1017/S0022112097006812 Published online by Cambridge University Press

along the normalized coordinate γ of particle streaks for the same experiment as figure 6(*a*); a corresponding interpretive sketch is given in figure 7(*b*). The vertical dimension of the photograph covers the approximate region from 10 cm below to 20 cm above the mid-depth of the fluid; the horizontal scale of the figure is also indicated. As mentioned above, corrections were made to minimize optical distortion due to the local curvature of the tank. The bright vertical band on the right of the photograph is due to light reflections from the shaft surface. Because the shaft is oscillating and the exposure time is longer than the shaft oscillation period, the edge of the band is approximately straight. Again, the motion direction of the particles is from dot to dash. Close inspection shows that in the vicinity of the shaft ($1 \lesssim \gamma \lesssim 4$), the motion appears fully turbulent. The particle trajectories have no preferred direction, indicating a three-dimensional motion which is not greatly affected by the background rotation. The motion field is approximately independent of the position along the cylinder (e.g. the turbulence intensity does not vary to a great extent), thus supporting the assumption that $\partial/\partial z = 0$ for statistically averaged fields. Away from the turbulent region ($4 \lesssim \gamma \lesssim 15$), the particle streaks continue to show irregular patterns, indicating that the motion field has a tendency to assume two-dimensionality in the presence of rotation with the characteristic horizontal length scale appearing to be somewhat larger than that in the vertical. Further away from the shaft ($15 \lesssim \gamma \lesssim 40$), clear dot-dash particle patterns are observed and, except near the upper and lower boundaries, the horizontal motion of the fluid dominates the vertical one. This observation is consistent with the Taylor–Proudman constraint. These large-scale motions away from the shaft are also random in space and time as ascertained from investigating sequential photographs for the same experiment (not shown).

To visualize the long-time behaviour of large-scale motions, dye tracers were used. Figure 8(*a–c*) is the top-view of sequential photographs of dye streaks released at $t = 0$ from the locations indicated for $S = 2.0$ cm, $\omega = 13.2$ rad s^{-1} and $f = 1.6$ rad s^{-1}. The fluid depth for this particular experiment was 24 cm and the photographs were taken at mid-depth. This arrangement allows one to have an entire view of the dye patterns while simultaneously keeping secondary motions, which occur near the test cell surface and floor, negligible. Note that on these photographs the inner 'heavy' bright circle is the light reflection from the shaft surface, and the outer 'light' bright circle is the reflection from the inner edge of the top Plexiglas plate. The dye release mechanism utilized a copper wire, of 0.1 cm diameter, stretched horizontally along a tank radius. To provide concentrated spots for dye release, small solder lumps were placed at selected locations along the wire. To facilitate discussions of the dye patterns, interpretive sketches of the corresponding dye images are given on the right in figure 8.

Figure 8(*a*) is a photograph taken 30 s after the dye tracer was released. Dye tracer patch α was released at $t = 0$ and has already been advected anticyclonically and is now approaching the highly turbulent region in the vicinity of the shaft where the dye pattern is not coherent. Dye tracer patch β, on the other hand, has been released at the time immediately preceding the photograph. It displays a meandering pattern and also advects anticyclonically. Note that dye tracer R, far away from the shaft and on the right of the picture, is a residual tracer from a previous experiment carried out under similar conditions. Although, the presence of patch R is rather fortuitous, it provides some information on the flow far away from the shaft.

In figure 8(*b*), at $t = 90$ s, dye-tracer patch α has moved to the lower-right of the shaft and has become mixed and diffused because of boundary turbulence. Also, the dye-tracer patch β is now in the vicinity of the shaft. Again, one observes that the dye

https://doi.org/10.1017/S0022112097006812 Published online by Cambridge University Press

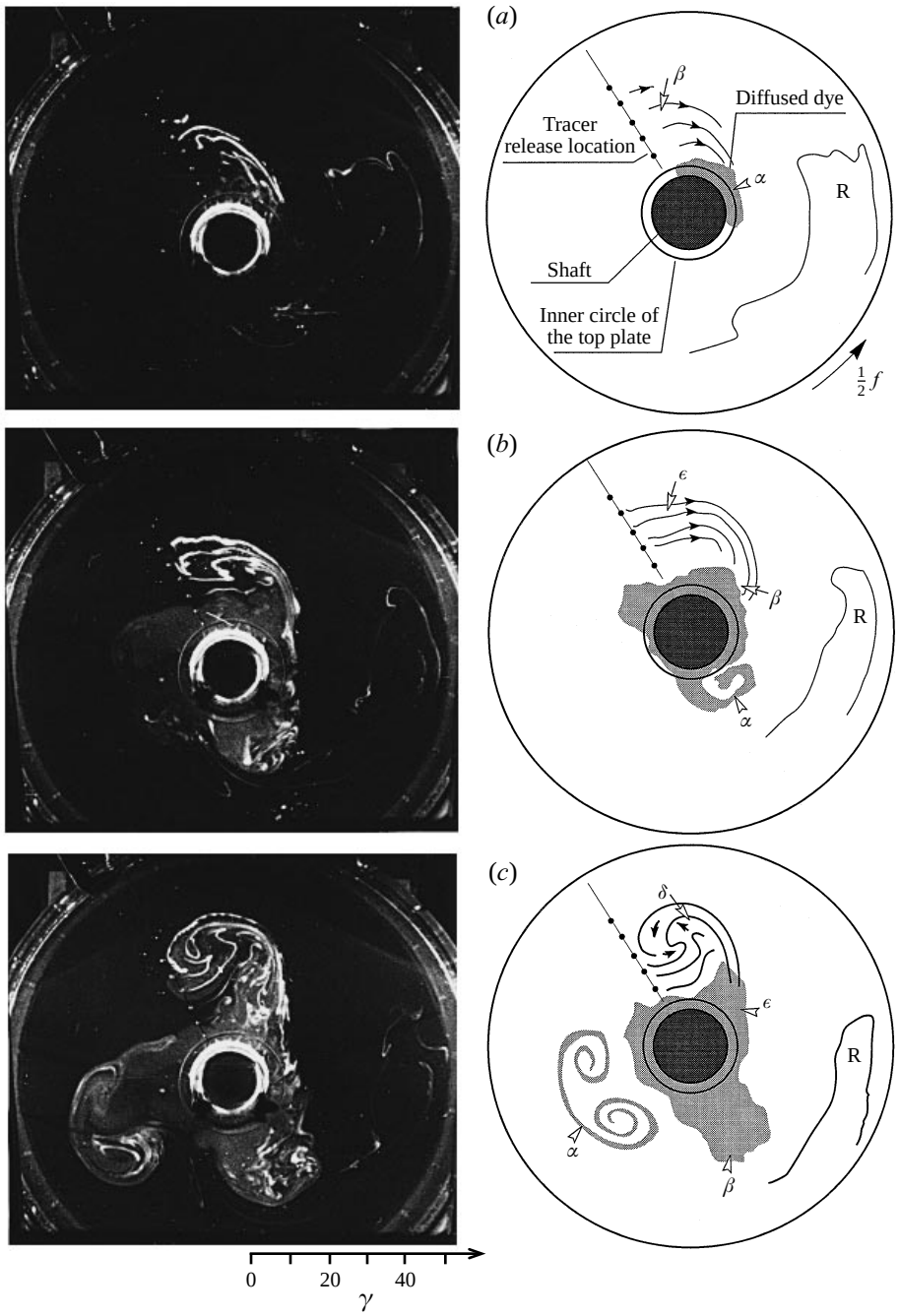


FIGURE 8. Dye-tracer photographs for $S = 2.0$ cm, $\omega = 13.2$ rad s^{-1} and $f = 1.6$ rad s^{-1}. The depth of the water is 24 cm. The tracer release was at $t = 0$ and for (*a*) $t = 30$ s, (*b*) 90 s and (*c*) 180 s. The exposure time is 1.0 s. The corresponding interpretive sketches are given on the right of the figures.

patterns near the shaft are highly diffused. The diffused dye quickly surrounds the shaft because of the existence of a mean anticyclonic flow in addition to turbulence. The width of the dye layer mixed by turbulence is limited. Figure 8(*b*) shows the release of a new dye-tracer patch ε. Similar to β in figure 8(*a*), tracer patch ε advects

https://doi.org/10.1017/S0022112097006812 Published online by Cambridge University Press

f (rad s^{-1})	κ	N
0	0.024	0.98
0.2	0.024	0.98
0.3	0.032	0.99
0.5	0.016	0.55
0.8	0.027	0.92
1.0	0.024	0.87
1.2	0.027	0.98
1.4	0.033	0.99
1.6	0.027	0.78

TABLE 2. Data fit of the normalized r.m.s. velocity against γ^{-1} (see relation (19)) for fixed $S = 2.0$ cm, $\omega = 24.5$ rad s^{-1} and various rotation rates. N is the correlation coefficient for the data fit

anticyclonically, displaying a meandering pattern. Residual tracer R continues to be visible. Note that the patch R drifts only in the θ direction, i.e. the radial mean flow is effectively zero. During the experiment, similar dye tracer patterns were observed above and below the mid-plane. These observations indicated that $U_r \approx 0$ is the central portions of the water column.

In figure 8(c), the time from the initial dye release is 180 s. One observes that α is now found on the lower-left portion of the shaft and at mid-radius of the test cell; it has now become a jelly-fish-like coherent structure. The motion of α suggests that there is not only an anticyclonic motion around the shaft but also some complex large-scale motion away from the turbulent boundary layer. This motion includes possible pinched-off dipole structures, as a result of barotropic instability of the mean motion around the shaft. Dye-tracer patch β occupies the position previously taken by α. The structure of β is diffused due to its proximity to the shaft. Dye-tracer patch ε is in the process of approaching, and moving anticyclonically around, the shaft. Also, newly released dye-tracer patch δ is forming a cyclonic structure after being advected downstream. The size of this coherent structure is approximately the same as the cross-section of the shaft. An approximate mean flow speed at the mid-radius is ~ 0.3 cm s^{-1} based on the evolution of α.

In summary, observations based on dye patterns suggest that (i) near the shaft the motion is fully turbulent, but is embedded in a mean anticylonic flow; (ii) away from the shaft, in the central portion of the test cell, the motion field consists of random cyclonic and anticyclonic vortices superimposed on a mean anticyclonic current (it is emphasized that tracers were sucked into or pinched off from the turbulent boundary layer randomly in space and time); and (iii) near the outer wall of the test cell, the motion is weak.

4.2.2. *Quantitative measurements*

The mean and r.m.s. velocities and the turbulent boundary layer thickness were measured for various rotation rates. Measurements of normalized r.m.s. velocities as a function of γ were made for experiments at fixed $S = 2.0$ cm and $\omega = 24.5$ rad s^{-1}; f was varied from 0.2 to 1.6 rad s^{-1}. Values of κ for various f and the data correlation coefficients are listed in table 2. It is seen that the coefficient κ of (19) is approximately constant and does not systematically depend on the rotation rate. Figure 9 shows a plot of the normalized r.m.s. velocities against γ for $S = 2.0$ cm, $\omega = 24.5$ rad s^{-1} and $f = 1.0$ rad s^{-1}. The components u_r, u_θ and w are indicated by different symbols and the

https://doi.org/10.1017/S0022112097006812 Published online by Cambridge University Press

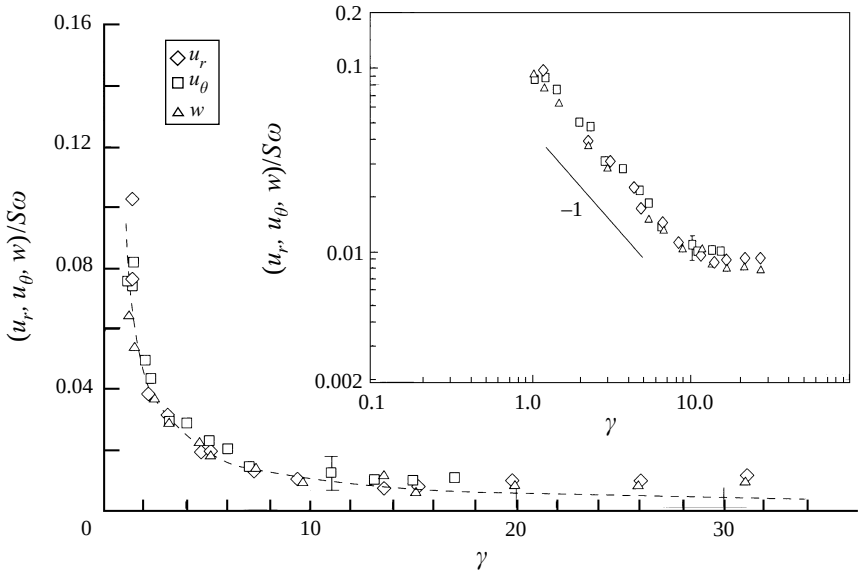


FIGURE 9. Normalized r.m.s. velocities versus γ for $S = 2.0$ cm, $\omega = 24.5$ rad s^{-1} and $f = 1.0$ rad s^{-1}. The insert is the log–log plot of the same data.

dashed line is a least-squares fit expressed by (19) with $\kappa \approx 0.024$. The insert in figure 9 is a log–log plot of the normalized r.m.s. velocities versus radial distance for the same data. The solid line represents a slope of -1. One observes that the r.m.s. velocities for $\gamma \lesssim 8$ follow the line with slope -1, while for $\gamma \gtrsim 8$, the r.m.s. values show different behaviour, presumably owing to large-scale motions in the mid-field and noise contamination. One concludes from the above observations that (i) in the near field, rotation does not affect the turbulence structure generated by the oscillating shaft and (ii) $u_r \sim u_\theta \sim w$ for the range of parameters considered, even in the presence of rotation. The $1/r$ decay of the r.m.s. velocity is consistent with (19) and the independence of r.m.s. velocities of rotation is expected because of the independence of $\overline{u_r' u_\theta'}$ of rotation in (13). The maximum Reynolds stress occurs close to the shaft, in an intense turbulent region where the local Rossby number $u/fd (\sim 10)$ is much larger than unity.

Figure 10 is a plot of the normalized mean velocity components $(U_r, U_\theta, W)/S\omega$ against γ for the experiment shown in figure 9. It is observed that the radial and vertical mean flows are effectively zero (within the error level of ± 0.005, normalized on $S\omega$) for all γ, while the azimuthal component varies from about $-.0.04$ to -0.02, for $0 \lesssim \gamma \lesssim 6$ and approaches zero for $\gamma \gtrsim 6$; the direction of U_θ is anticyclonic and the magnitude generally decreases with the radial coordinate. Note that, while the r.m.s. velocities experience a rapid decay with increasing distance from the boundary in the vicinity of the shaft ($0 \lesssim \gamma \lesssim 10$), the mean velocity U_θ does not vary significantly in the region $3 \lesssim \gamma \lesssim 7$; see figure 10. This can be attributed to the effective radial exchange of momentum in that region, where the turbulence tends to distribute the mean momentum uniformly.

Measurements of the turbulent boundary layer thickness were made by photographing rheoscopic particle images over the vertical range of $z \approx \pm 5$ cm for the rotating experiments. A vertical light sheet (0.5 cm wide) along a tank radius was employed to illuminate a vertical section, and side-view photographs of rheoscopic patterns were thus obtained. In the turbulent region near the shaft, rheoscopic patterns

https://doi.org/10.1017/S0022112097006812 Published online by Cambridge University Press

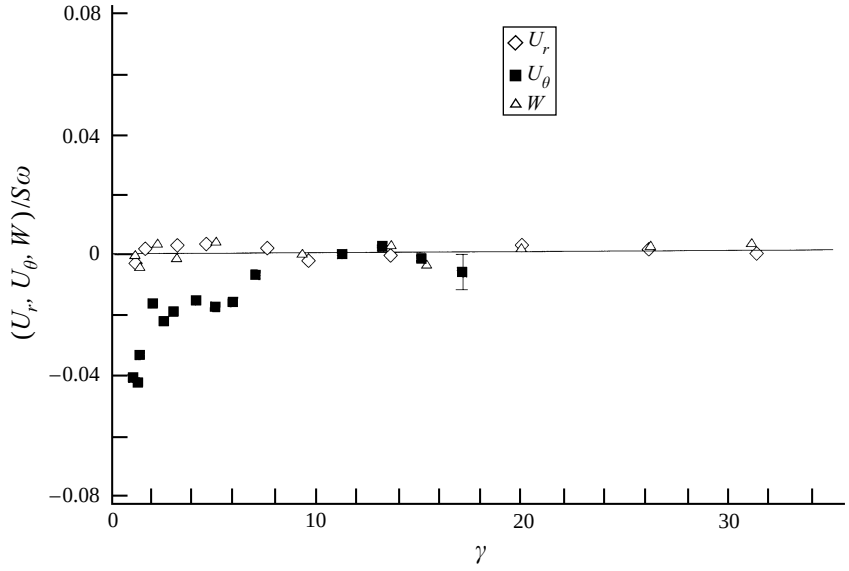


FIGURE 10. Normalized mean velocities versus γ for the same experiment as in figure 9.

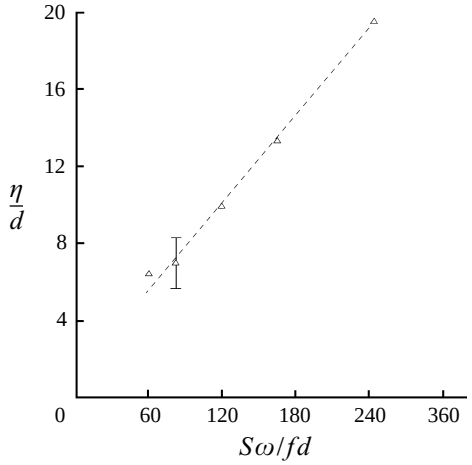


FIGURE 11. Normalized turbulent boundary layer thickness η/d versus $S\omega/fd$ for $S = 2.0$ cm and $\omega = 24.5$ rad s^{-1}.

are displayed as short random bright and dark images, while in the mid-field, large-scale bright–dark patterns were observed. The radial distance at which a rheoscopic image changes quickly from a short- to a large-scale pattern was taken to be the approximate width of the turbulent region. This measurement is somewhat subjective and the error (the uncertainty in determining the boundary layer thickness) was estimated to be of the order of 20%. It was observed that the larger the Coriolis parameter, other parameters being fixed, the thinner the turbulent boundary layer. Again, observations of the rheoscopic particle images indicated a boundary layer structure independent of the vertical coordinate.

Figure 11 is a plot of the normalized turbulent boundary layer thickness η/d against $S\omega/fd$ for experiments carried out with $S = 2.0$ cm and $\omega = 24.5$ rad s^{-1}. The dashed line indicates the linear fit to the data, which shows an approximately linear

https://doi.org/10.1017/S0022112097006812 Published online by Cambridge University Press

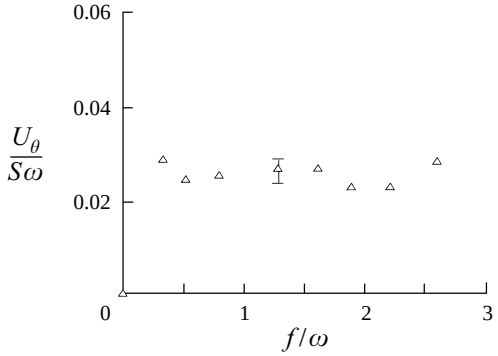


FIGURE 12. Normalized mean azimuthal velocity versus Ro_t^{-1} for $S = 2.0$ cm, $\omega = 24.5$ rad s^{-1} and at a fixed $\gamma = 3.0$.

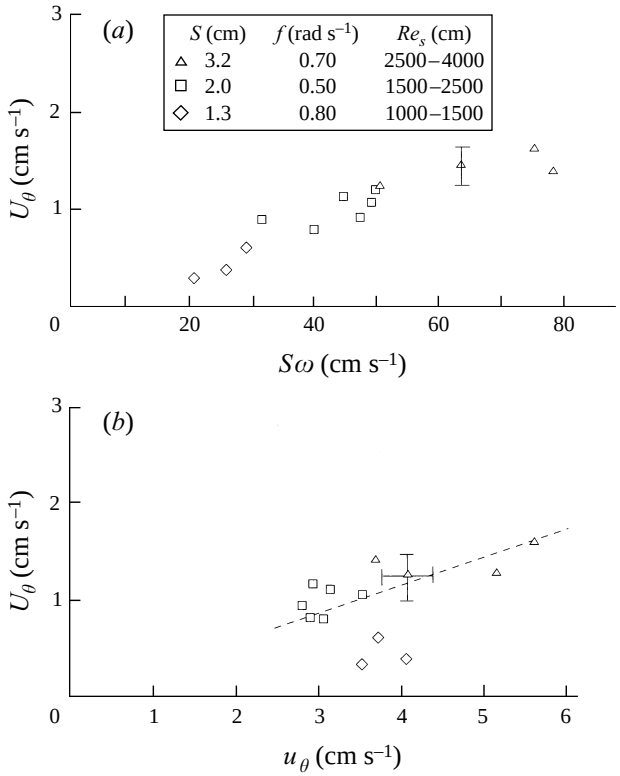


FIGURE 13. (*a*) Mean anticyclonic velocity versus $S\omega$ at a fixed $\gamma = 3.0$ for various stroke and Coriolis parameter values; (*b*) mean anticylonic velocity versus r.m.s. velocity for the same experiments as in (*a*).

dependence between η/d and $S\omega/fd$. This result is consistent with previous observations by Dickinson & Long (1983) and Hopfinger *et al.* (1982) that $\eta = \beta u/f$ (i.e. relation (15)).

Variations of U_θ for various rotation rates were also considered. Figure 12 is a plot of the normalized mean azimuthal velocity $U_\theta/S\omega$ against the inverse temporal Rossby number $Ro_t^{-1} = f/\omega$. Here the stroke, $S = 2.0$ cm, and the shaft oscillation frequency, $\omega = 24.5$ rad s^{-1}, were fixed and U_θ was measured at a given radial location $\gamma = 3.0$.

https://doi.org/10.1017/S0022112097006812 Published online by Cambridge University Press

The results suggest that $U_\theta/S\omega$ is independent of the rotation rate for the ranges of the parameter values considered, an observation consistent with (16). As $f/\omega \to 0$, one clearly would expect $U_\theta/S\omega \to 0$; unfortunately, it was not possible to investigate sufficiently small f/ω to study this region of parameter space with the present experimental facility.

Figure 13(*a*) depicts a plot of U_θ versus $S\omega$ for the set of experimental parameters given in the legend; the velocities are measured at the radial location $\gamma = 3$. It is seen that the anticyclonic rectified current is approximately linearly dependent on $S\omega$. In order to investigate the relation between the turbulent intensity (i.e. r.m.s. velocities) and the mean flow in the turbulent boundary layer, a plot of the mean flow U_θ versus the r.m.s. velocity u_θ was constructed. The results are given in figure 13(*b*) for the same experimental data as used for figure 13(*a*); the dashed line represents a rough estimate of the relation between U_θ and u_θ. Note that the data show a straight line trend, except the run with $S = 1.3$ cm, for which the Reynolds number (1000–1500) may have been too low to yield appreciable turbulence levels. Thus, we may expect, on average, the mean velocities to be approximately 20–30% of the r.m.s. velocity levels for the experiments considered.

5. Discussion and concluding remarks

Laboratory experiments were conducted on boundary-induced turbulence in a homogeneous fluid in the presence of background rotation. The turbulence was generated by a vertically oscillating shaft, and its statistics were shown to be approximately vertically independent over a major portion of the test cell. The turbulence intensities were found to increase linearly with $S\omega$, and decrease with increasing radial distance. Near the shaft, rotation does not affect the turbulence structure, i.e. the turbulence characteristics are the same for both the rotating and the non-rotating experiments. The Rossby number in the immediate vicinity of the shaft is estimated as $Ro = u/fd \sim 10$, with $u \sim 5$ cm s^{-1}, $f \sim 1.0$ s^{-1} and $d = 0.5$ cm; the effects of rotation are thus not expected to be of leading-order importance in this region. Furthermore, the turbulence is found to have the property $u_r \approx u_\theta \approx w$. For a given flow configuration, the normalized r.m.s. velocity decays with the dimensionless distance from the boundary as $u/S\omega \propto \gamma^{-1}$, where $\gamma = (r - r_0)/d$. In the mid-radius of the tank, the turbulence is weak and the motion is characterized by random large-scale anticyclonic and cyclonic vortices as well as an anticyclonic mean flow. Because the flow velocities are small and the motion scale is large at the mid-radius, the Rossby number of the large-scale motion is much smaller than unity: the flow is dominated by rotation and tends to be horizontal.

An anticyclonic rectified (mean) flow U_θ was found to develop around the oscillating shaft in the presence of rotation. This flow is approximately uniform within the turbulent boundary layer for the range $3 \lesssim \gamma \lesssim 7$. The normalized turbulent boundary layer thickness η/d was found to vary linearly with $S\omega/fd$.

Consideration of the equations of motion indicates that no mean flow should be expected for the non-rotating case. In the presence of rotation, however, those same equations indicate that an anticyclonic flow in the vicinity of the cylinder shaft can be initiated, grow and be maintained by Reynolds stress gradients which are essentially independent of rotation. The laboratory observations are qualitatively in accord with the arguments advanced. Although the generation of mean swirls by small-scale turbulence in the presence of background rotation has been observed in several previous experiments, to our knowledge this is the first experimental demonstration

https://doi.org/10.1017/S0022112097006812 Published online by Cambridge University Press

wherein it was shown that the gradients of Reynolds stresses can indeed generate an organized mean circulation.

In the present study, a cylindrical geometry was chosen for geometrical simplicity to exemplify one aspect of the complex problem of oceanic rectified flows and to elucidate relevant physics. In general, mean flow generation by turbulence occurs in complex geometries where non-zero horizontal turbulent gradients exist in the presence of rotation. Examples may be coastlines and long shelf-breaks where the intensity of boundary turbulence decreases with increasing distance from the boundaries. In the case of a straight boundary, relations (6)–(8) still hold with the centrifugal force playing an insignificant role. In such cases, a mean flow is expected to be generated along the boundary. The direction of the mean flow should be such that the region of strong turbulence is on the right-hand side, facing downstream. The present study suggests that small-scale turbulent motions can convert energy into large-scale motions such as rectified currents. This phenomenon can have applications to a range of environmental problems, for example the long-term transport of passive scalars in coastal oceans.

This work was mainly supported by the Physical Oceanography Program of the National Science Foundation under Grant number OCE-9301572; that support is gratefully acknowledged. Support of the Ocean Sciences Division of the U.S. Office of Naval Research and the Fluid Mechanics and Hydraulics Program of the NSF is also recognized. The authors also wish to thank the anonymous reviewers for their helpful suggestions for improving the manuscript.

REFERENCES

Bardina, J., Ferziger, J. H. & Rogallo, R. S. 1985 Effects of rotation on isotropic turbulence: Computation and modelling. *J. Fluid Mech.* **154**, 321–336.

Bartello, P., Métais, O. & Lesieur, M. 1994 Coherent structures in rotating three-dimensional turbulence. *J. Fluid Mech.* **273**, 1–29.

Bidokhti, A. A. & Tritton, D. J. 1992 The structure of a turbulent free shear layer in a rotating fluid. *J. Fluid Mech.* **241**, 469–502.

Boyer, D. L., Chabert D'Hières, G., Didelle, H., Verron, J., Chen, R. & Tao, L. 1991 Laboratory simulation of tidal rectification over seamounts, homogeneous model. *J. Phys. Oceanogr.* **21**, 1559–1579.

Bretherton, F. P. & Haidvogel, D. B. 1976 Two-dimensional turbulence above topography. *J. Fluid Mech.* **78**, 129–154.

Bretherton, F. P. & Turner, J. S. 1968 On the mixing of angular momentum in a stirred rotating fluid. *J. Fluid Mech.* **32**, 449–464.

Butman, B., Beardsley, R. C., Magnell, B., Frye, D., Vermersch, J. A., Schlitz, R., Limeburner, R., Wright, W. R. & Noble, M. A. 1982 Recent observations of mean circulation on Georges Bank. *J. Phys. Oceanogr.* **12**, 569–591.

Chen, C. & Beardsley, R. C. 1995 A numerical study of stratified rectification over finite-amplitude banks. Part I: symmetric banks. *J. Phys. Oceanogr.* **25**, 2090–2110.

Collin de Verdiere, A. 1980 Quasi-geostrophic turbulence in a rotating homogeneous fluid. *Geophys. Astrophys. Fluid Dyn.* **15**, 23–251.

Dickinson, S. C. & Long, R. R. 1983 Oscillating grid turbulence including effects of rotation. *J. Fluid Mech* **126**, 315–333.

Eriksen, C. 1991 Observations of amplified flows atop a large seamount. *J. Geophys. Res* **96**, 15227–15236.

Fernando, H. J. S. & De Silva, P. D. 1993 Note on secondary flows in oscillating-grid, mixing-box experiments. *Phys. Fluids* A **5**, 1849–1851.

Garreau, P. & Mazé, R. 1992 Tidal rectification and mass transport over a shelf break: a barotropic frictionless model. *J. Phys. Oceanogr.* **22**, 719–731.

https://doi.org/10.1017/S0022112097006812 Published online by Cambridge University Press

Genin, A., Noble, M. & Lonsdale, P. F. 1989 Tidal currents and anticyclonic motions on two North Pacific seamounts. *Deep-Sea Res.* **36**, 1803–1815.

Gough, D. O. & Linden-Bell, D. 1968 Vorticity expulsion by turbulence: astrophysical implications of an Alka-Seltzer experiment. *J. Fluid Mech.* **32**, 437–447.

Holloway, G. 1987 Systematic forcing of large-scale geophysical flows by eddy-topography interaction. *J. Fluid Mech.* **184**, 463–476.

Honji, H., Taneda, S. & Tatsuno, A. 1980 Some practical details of the electrolytic precipitation method of flow visualization. *Res. Int. Appl. Mech.* **2**, 83–89.

Hopfinger, E. J. 1989 Turbulence and vortices in rotating fluids. In *Theoretical and Applied Mechanics* (ed. P. Germain, M. Piau & D. Caillerie), pp. 117–138. Elsevier.

Hopfinger, E. J., Browand, F. K. & Gagne, A. 1982 Turbulence and waves in a rotating tank. *J. Fluid Mech.* **125**, 505–534.

Hopfinger, E. J. & Toly, J.-A. 1976 Spatially decaying turbulence and its relation to mixing across density interfaces. *J. Fluid Mech.* **78**, 155–175.

Ibbetson, A. & Tritton, D. J. 1975 Experiments on turbulence in a rotating fluid. *J. Fluid Mech.* **68**, 639–672.

Maas, L. R. M. & Zimmerman, J. T. F. 1989*a* Tidal-topography interaction in a stratified shelf sea. I. Basic equations for quasi-nonlinear internal tides. *Geophys. Astrophys. Fluid Dyn.* **45**, 1–35.

Maas, L. R. M. & Zimmerman, J. T. F. 1989*b* Tidal-topography interaction in a stratified shelf sea. II. Bottom trapped internal tides and baroclinic residual currents. *Geophys. Astrophys. Fluid Dyn.* **45**, 37–69.

McEwan, A. D. 1973 Laboratory demonstration of angular momentum mixing. *Geophys. Fluid Dyn.* **5**, 283–311.

McEwan, A. D. 1976 Angular momentum diffusion and the imitation of cyclones. *Nature* **260**, 126–128.

Métais, O., Flores, C., Yanase, S., Riley, J. J. & Lesieur, M. 1995 Rotating free-shear flows. Part 2. Numerical simulations. *J. Fluid Mech.* **293**, 47–80.

Plumb, R. A. & McEwan, A. D. 1978 The instability of a forced standing wave in a viscous stratified fluid: A laboratory analogue of the quasi-biennial oscillation. *J. Atmos. Sci.* **35**, 1827–1839.

Scorer, R. S. 1965 Vorticity in nature. *Department of Mathematics, Imperial College, London, Rep.*

Scorer, R. S. 1966 Origin of cyclones. *Sci. J.* **2**, 46–52.

Zhang, X. & Boyer, D. L. 1993 Laboratory study of rotating, stratified, oscillatory flow over a seamount. *J. Phys. Oceanogr.* **23**, 1122–1141.

Zhang, X., Boyer, D. L., Chabert D'Hières, G. & Aelbrecht, D. 1994 Rectified flow of a rotating fluid along a vertical side wall. *Phys. Fluids* **6**, 1440–1453.

Zhang, X., Boyer, D. L., Chabert D'Hières, G., Aelbrecht, D. & Didelle, H. 1993 Rectified flow along a vertical coastline. *Dyn. Atmos. Oceans* **19**, 115–145.

Zimmerman, J. T. F. 1978 Topographic generation of residual circulation by oscillatory (tidal) currents. *Geophys. Astrophys. Fluid Dyn.* **11**, 34–47.

https://doi.org/10.1017/S0022112097006812 Published online by Cambridge University Press